Stabilization mechanisms of various acoustic metasurfaces on the second mode in hypersonic boundary-layer flows ⊘

Xiao Liu (刘潇) [ID] ; Ying Dong (董颖); Tiehan Long (龙铁汉) [ID] ; Rui Zhao (赵瑞) ✉ [ID] ; Chihyung Wen (温志湧) [ID]

Check for updates

View Online   Export Citation

Articles You May Be Interested In

Mechanism of stabilization of porous coatings on unstable supersonic mode in hypersonic boundary layers

Physics of Fluids (May 2021)

Secondary instability of stationary Görtler vortices originating from first/second Mack mode

Physics of Fluids (March 2020)

Scattering of Mack modes by solid-porous junctions in hypersonic boundary layers

Physics of Fluids (August 2022)

Stabilization mechanisms of various acoustic metasurfaces on the second mode in hypersonic boundary-layer flows

View Online   Export Citation   CrossMark

Xiao Liu (刘潇),[1] (iD) Ying Dong (董颖),[2] Tiehan Long (龙铁汉),[3] (iD) Rui Zhao (赵瑞),[1,a] (iD) and Chihyung Wen (温志湧)[4] (iD)

AFFILIATIONS

[1]School of Aerospace Engineering, Beijing Institute of Technology, Beijing 100081, China
[2]Beijing Aerospace Technology Institute, Beijing 100074, China
[3]China Academy of Aerospace Aerodynamics, Beijing 100074, China
[4]Department of Aeronautical and Aviation Engineering, The Hong Kong Polytechnic University, Hung Hom, Kowloon, Hong Kong, China

[a]Author to whom correspondence should be addressed: zr@bit.edu.cn

ABSTRACT

Acoustic metasurfaces have been shown to stabilize the Mack second mode in the hypersonic boundary layer through various acoustic wave manipulations, but the stabilization mechanisms still lack unified clarification. In the present work, momentum potential theory is used to develop a physics-based analysis of the perturbance flow field above three kinds of acoustic metasurfaces: the absorptive, impedance-near-zero, and reflection-controlled metasurfaces. It found the thermal-acoustic source term P_{ta} contributes the most to the instability, and the main differences in the stabilization mechanisms of the various metasurfaces can be derived from the distributions of P_{ta}. The absorptive metasurface largely restrains the negative P_{ta} term near the surface and slightly attenuates it near the critical layer. The impedance-near-zero metasurface generates a positive contour under the critical layer, while the reflection-controlled metasurface induces additional positive P_{ta} intertwining along the critical layer. In addition, a uniform macroslit surface without particular acoustic characteristic is verified to stabilize the Mack second mode because the recirculation zones inside the macroslits attenuate the near-surface negative P_{ta}. By deflecting the reflective waves, additional larger positive P_{ta} could be produced and wrapped along the critical layer and that achieves a more prominent stabilization performance by designing a reflection-controlled macroslit surface.

Published under an exclusive license by AIP Publishing. https://doi.org/10.1063/5.0165938

I. INTRODUCTION

The transition from laminar to turbulent flow causes a significant increase in aerodynamic heat and skin friction, which poses a challenge to the thermal protection system (TPS) of hypersonic vehicles.[1–3] In high-attitude environments with small disturbances, the Mack second mode is considered to exhibit highest growth rate and, thus, dominates the transition process,[4] especially for cruise vehicles with predominantly two-dimensional (2D) leading edges.[1] Additionally, the Mack second mode induces an additional peak heat transfer that is slightly higher than that in the turbulent region.[5] Therefore, effective suppression of the amplification of the Mack second mode could inhibit the boundary-layer (BL) transitions and reduce heat transfer in the TPS. The Mack second mode behaves like a trapped acoustic mode propagating in a waveguide between the wall and the relative sonic line, where the convective Mach number $Ma_c = \frac{u(y)-c}{a(y)} = 1$.

Here, $u(y)$ is the mean velocity, c is the disturbance phase speed, and $a(y)$ is the local sound speed.[4,6] The acoustic wave changes dynamically from a compression wave to an expansion wave, and vice versa, in this relative supersonic region. Its wavelength is approximately twice the BL thickness, with a relatively high frequency that corresponds to the ultrasonic band in hypersonic boundary layer (HBL) flows.[7] Malmuth et al.[8] proposed the hypothesis that an ultrasonic absorptive coating (UAC) could suppress the Mack second mode due to its acoustic-wavelike behavior, with the mechanism being that the UAC dissipates the acoustic disturbance energy through the viscosity in the narrow microslits and, therefore, stabilizes the HBL. Fedorov and Malmuth[7] used linear stability analysis (LST) to verify this stabilization effect by conducting parametric studies of an UAC with equally spaced cylindrical blind micropores in a Mach 6 BL flow. Rasheed et al.[9] observed that the UAC could delay the transition under a broad

13 January 2025 02:57:43

range of inflow Reynolds numbers for a cone model in a Mach 5 piston-driven shock tunnel. For most of the runs, the laminar BL was sustained up to the model end on the UAC surface, whereas a transition on the rigid surface was observed halfway along the cone surface. Their pioneering work has sparked extensive studies on this passive transition control technology using LST,[10,11] direct numerical simulation (DNS),[12–18] and wind tunnel experimental research.[19–24] It was also found that most porous materials with characteristic micropore diameters much less than 1 mm, such as felt-metal,[23] carbon–carbon (C/C),[24] and permeable steel,[22] have a stabilization effect similar to that of the UAC. To explore the potential of porous materials, Zhao et al.[25,26] broadened the UAC concept to an acoustic metasurface to suppress the Mack second mode. Acoustic metasurfaces are planar metamaterial structures constructed with monolayer or multilayer stacks of subwavelength building blocks, which significantly broaden the horizon of acoustic wave manipulation from wavefront modulation[27,28] to sound insulation and absorption.[29–31] In this sense, the UAC is a type of acoustic metasurface that dissipates disturbance energy via its absorption characteristics. However, the metasurface concept has provided more possibilities for controlling the propagation of the Mack second mode. Zhao et al.[25] designed an impedance-near-zero acoustic metasurface capable of effectively suppressing the Mack second mode via the out-of-phase behavior between the incident and reflected waves. The DNS results showed that the typical "two-cell" structure of the Mack second mode was divided in the slit and above the surface. Recently, Zhao et al.[26] proposed reflection-controlled acoustic metasurfaces composed of periodical subwavelength slit groups that can change the reflection direction of acoustic waves. This metasurface divided the mode structure into several small parts, and therefore, largely inhibited the growth of the Mack second mode.

Although the stabilization effects of various acoustic metasurfaces on the HBL have been revealed, the physics-based explanations for these different stabilization mechanisms remain ambiguous. The difficulty in elucidating the stabilization mechanisms stems from the lack of a universal definition of an "acoustic wave" in the HBL, which exhibits a strong gradient in the mean flow field. For a compressible, viscous, and heat-conductive uniform flow field, Kovásznauy[32] proposed a split theorem that decomposes random fluctuations into three different modes: the vorticity, entropy, and acoustic modes. In the linear stage, these three modes obey three independent governing equations, and the interactions between different modes can be ignored. Unfortunately, Kovásznauy's approach is not applicable for nonuniform flow fields. Doak's momentum potential theory (MPT) provides an elegant tool for decomposing a time-stationary fluctuation flow field into three different components, which overcomes the restrictions of Kovásznauy's approach in inhomogeneous systems.[33,34] It should be noted the decomposition into constituent modes can be performed on any flow as long as it satisfies conditions of statistical stationarity and the continuum approximation.[35] Therefore, it is suitable for the investigation of the stabilization mechanisms of instabilities in the HBL. In Doak's approach, the momentum density field, $\rho\boldsymbol{u}$, is decomposed into the corresponding vortical, acoustic, and thermal components using Helmholtz decomposition. The vortical component contains all rotational motion, while the irrotational component is divided into acoustic (irrotational and isentropic) and thermal (irrotational and isobaric) components. Furthermore, an energy corollary for the total fluctuating enthalpy (TFE) is derived. This energy corollary

helps to define the generation and transport of the TFE in the flow field, which provides a causal interpretation for the development of disturbances. Tumuklu et al.[36] studied unsteadiness of axisymmetric shock-dominated hypersonic laminar separated flow over a double cone with MPT. The acoustic components show a sign change downstream of the bow shock, and the magnitude of the thermal components is approximately a factor of 5 lower in comparison to the acoustic counterparts. The striation patterns in the vorticity field shown in the shear layer region and downstream of the bow shock are consistent with those in the thermal components fields. Unnikrishnan and Gaitonde[35,37] applied Doak's approach to decompose the instability modes in a Mach 6 BL flow, which they referred to as fluid-thermodynamic (FT) decomposition. Specifically, the discrete modes in the LST and DNS results of linear and nonlinear saturated disturbances were decomposed into different components. The decomposition of the LST results showed that in the linear regime, each discrete mode contained all the FT components. For the DNS results, a rope-shaped recirculation-cell pattern was observed in the contour of the vortical component across the generalized inflection point (GIP), and a "trapped" structure was produced in both the acoustic and thermal components. The TFE source mechanisms were studied by considering the instantaneous streamwise distribution of various source terms in the vicinity of the amplification of the Mack second mode. Houston et al.[38] preformed FT decomposition to separate disturbances into their vortical, thermal, and acoustic components. For both the flat plate and blunt cone, the vortical components were found to be largest, followed by the thermal and acoustic components. Long et al.[39] clarified the mechanism of the UAC in the suppression of supersonic mode instability in the HBL by using Doak's approach. The DNS results of Mach 6 flat-plate flows on rigid walls and the UAC were decomposed into vortical, acoustic, and thermal components. The source terms and fluxes were studied based on their corresponding energy corollaries. Compared to the rigid wall, the UAC significantly suppressed the vortical source near the surface, resulting in less vortical energy being transformed into acoustic energy. The acoustic energy was eventually exhausted due to energy loss in the outward transport of the TFE, and the "sound radiation" of the supersonic mode disappeared. Long et al.[40] conducted an energy analysis of the key sources responsible for the modal growth in the MPT framework. The thermal-acoustic source is revealed to be the most significant cause of the second-mode instability in the HBL. The thermal-acoustic source is further decomposed into the dissipative part and the nondissipative part. The dissipative thermal-acoustic source has a dominant effect on the amplification of the second mode near the wall surface. The nondissipative thermal-acoustic source affects the growth of second mode significantly at the critical layer [where $\frac{u(y)-c}{a(y)} = 0$].

The goal of the present work is to use Doak's MPT to provide a physical interpretation of the differences in the stabilization mechanisms of the absorptive, impedance-near-zero, and reflection-controlled metasurfaces. After numerically simulating the flow field, the fluctuating momentum density fields on the rigid surface and the acoustic metasurfaces are decomposed into vortical, acoustic, and thermal components. The contributions of source terms to the growth rate of the Mack second mode are clarified, and the source mechanisms of the different surfaces are compared. In addition, two types of macroslit surfaces are introduced and their stabilization mechanisms are also discussed under Doak's MPT framework.

II. MOMENTUM POTENTIAL THEORY

Similar to the authors' earlier work, it considers the Mack second mode traveling in the HBL along a 2D flat-plate with or without metasurfaces at a zero angle of attack.[17,18] The metasurfaces were all corrugated with subwavelength slits (2D cavities). Because of the 2D geometry and 2D flow nature considered, the 2D MPT was adopted in the research on stabilization mechanisms of various acoustic metasurfaces.[25,40] To clarify the context, Doak's MPT is summarized as follows: The momentum density $m\,(\equiv \rho u)$ is selected as the primary dependent vector field to be decomposed. The fluctuation momentum density m' can be expressed as a superposition of the vortical component m'_B, acoustic component m'_A, and thermal component m'_T. The superscript $'$ denotes fluctuation variables,

$$m' = m'_B + m'_A + m'_T. \tag{1}$$

The energy budget for the total fluctuating enthalpy (TFE), $H' = \left(C_p T + \frac{u \cdot u}{2}\right)'$, is another critical aspect of Doak's MPT approach. The perturbation of the product of two variables q and k is: $(qk)' = q'\bar{k} + \bar{q}k' + q'k'$. The mean transport equation of the TFE due to m' can be written as follows:

$$\nabla \cdot \overline{H'm'} = -\overline{m' \cdot \alpha'} + \frac{\overline{p' \frac{\partial S'}{\partial t}}}{R}, \tag{2}$$

where $\overline{H'm'}$ is the mean TFE flux, which represents the TFE transported by m' in a time-stationary process. $\bar{q}$ represents the time-average of variable q. α' denotes the acceleration vector, and S denotes entropy. Substituting Eq. (1) into Eq. (2) yields

$$\frac{\partial \overline{(\rho u)'H'}}{\partial x} + \frac{\partial \overline{(\rho v)'H'}}{\partial y} = -\left[\overline{m'_B \cdot \alpha'} + \overline{m'_A \cdot \alpha'} + \overline{m_T' \cdot \alpha'}\right] + \frac{\overline{p' \frac{\partial S'}{\partial t}}}{R}. \tag{3}$$

The left-hand-side terms in Eq. (3) are the energy flux terms that represent the fluctuation energy transported along the streamwise and normal directions by the flow. The first three terms on the right-hand side indicate the various sources of the interaction of the vector α' with different components. In addition to the source terms due to the MPT components, according to Ref. 40, the source term $\frac{p' \frac{\partial S'}{\partial t}}{R}$ represents the thermo-acoustic coupling effect in the disturbances flow field. For convenience of discussion, the vortical source $-\overline{m'_B \cdot \alpha'}$, acoustic source $-\overline{m'_A \cdot \alpha'}$, and thermal source $-\overline{m'_T \cdot \alpha'}$ are designated as P_B, P_A, and P_T, respectively. The source due to the thermo-acoustic coupling effect is designated as P_{ta}.

For the streamwise growth rate based on the DNS results of the rigid surface,

$$\sigma_r = \frac{\int_0^{+\infty} P_A dy + \int_0^{+\infty} P_B dy + \int_0^{+\infty} P_T dy + \int_0^{+\infty} P_{ta} dy}{2\int_0^{+\infty} \overline{(\rho u)'H'} dy}, \tag{4}$$

where σ_r is the growth rate of the unstable mode, and the contributions of the source terms P_A, P_B, P_T, and P_{ta} to the growth rate are
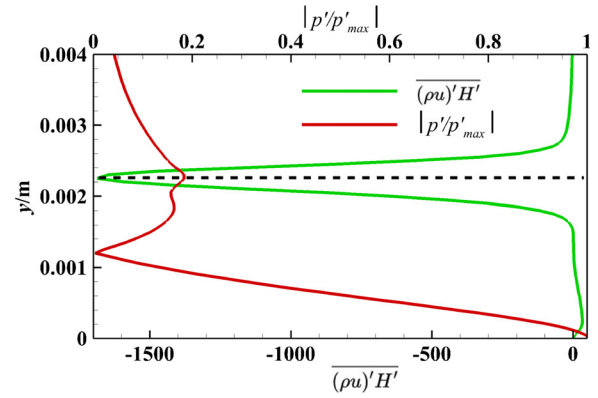

FIG. 1. Normalized distributions of $\overline{(\rho u)'H'}$ [unit: kg/(s³)] and fluctuating pressure at $x = 0.15$ m. The critical layer is marked using a dashed line.

$$\sigma_{rj} = \frac{\int_0^{+\infty} P_j dy}{2\int_0^{+\infty} \overline{(\rho u)'H'} dy}. \tag{5}$$

The subscript j represents A, B, T, or ta, and therefore, $\sigma_r = \sigma_{rA} + \sigma_{rB} + \sigma_{rT} + \sigma_{rta}$. Figure 1 shows the wall normal distributions of $\overline{(\rho u)'H'}$ term and fluctuating pressure at $x = 0.15$ m. $\overline{(\rho u)'H'}$ is negative near the critical layer, and the disturbance peak is observed in this region. Because $\int_0^{+\infty} \overline{(\rho u)'H'} dy < 0$, negative P_i terms could lead to positive σ_{rj} terms, causing instability in the HBL.

For the DNS of an acoustic metasurface with a regular periodic microstructure, integrating Eq. (3) in a periodic unit cell (Fig. 2),

$$\int_{y_w}^{+\infty} \int_x^{x0} \left(\frac{\partial \overline{(\rho u)'H'}}{\partial x} + \frac{\partial \overline{(\rho v)'H'}}{\partial y}\right) dx dy$$
$$= \oiint P_A dx dy + \oiint P_B dx dy + \oiint P_T dx dy + \oiint P_{ta} dx dy, \tag{6}$$

where s is the period of the microstructure, and $y_w = 0$ for the rigid part, and $y_w = -h$ indicating the bottom of slits. Since $(\rho v)' = 0$ for
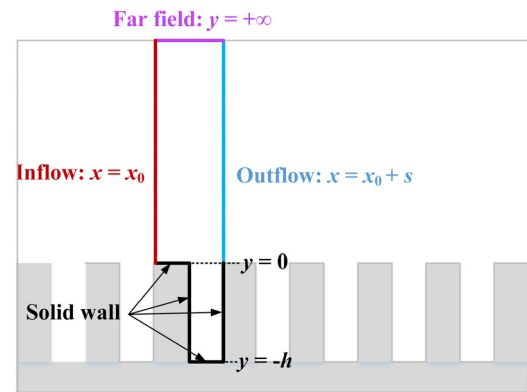

FIG. 2. Schematic of the integration area of a periodic unit cell.

$y = y_w$ and $y \to \infty$, the MPT energy budget equation in two-dimensional integral form within a period is derived as follows:

$$\int_{y_w}^{+\infty} \overline{(\rho u)' H'} dy \Big|_{x_0}^{x_0+s} = \oiint P_A dxdy + \oiint P_B dxdy + \oiint P_T dxdy$$
$$+ \oiint P_{ta} dxdy. \tag{7}$$

Since the mean flow field over the acoustic metasurface is periodic, the growth rate σ_m satisfies

$$\int_{y_w}^{+\infty} \overline{(\rho u)' H'} dy \Big|_{x_0+s} = e^{2\sigma_m s} \int_{y_w}^{+\infty} \overline{(\rho u)' H'} dy \Big|_{x_0}. \tag{8}$$

As a result,

$$\sigma_m = \frac{1}{2s} ln \left(\frac{\int_{y_w}^{+\infty} \overline{(\rho u)' H'} dy \Big|_{x_0+s}}{\int_{y_w}^{+\infty} \overline{(\rho u)' H'} dy \Big|_{x_0}} \right). \tag{9}$$

From Eq. (9), we can derive the contribution of each source term to σ_m,

$$\sigma_{mj} = \frac{1}{2s} ln \left(\frac{\oiint P_j dxdy}{\int_{y_w}^{+\infty} \overline{(\rho u)' H'} dy \Big|_{x_0}} + 1 \right). \tag{10}$$

The Doak's MPT method is applied to present an explanation of the differences in the stabilization mechanisms of three types of meta-surfaces. Before performing the MPT decomposition, DNS had been conducted for Mach 6 BL flows on rigid plate surface and acoustic metasurfaces[25,26,43] (Fig. 3). The flow conditions are set to be similar to those described in Bountin et al.[41] In all cases, the freestream Mach number Ma_∞ is 6, the freestream unit Reynolds number is $10.5 \times 10^6 \, \text{m}^{-1}$, the freestream temperature is $T_\infty = 43.18 \, \text{K}$, and the wall is isothermal with $T_w = 293 \, \text{K}$. The perfect gas condition was assumed, with Prandtl number, $Pr = 0.72$, and the ratio of specific heats, $\gamma = 1.4$. The dynamic viscosity μ was calculated by applying Sutherlands law in the form $\mu = \mu_\infty (T/T_\infty)^{3/2} (T_s/T_\infty + 1)/(T_s/T_\infty + T/T_\infty)$, where $T_s = 110 \, \text{K}$, and the freestream dynamic viscosity $\mu_\infty = 2.69 \times 10^{-6} \, \text{kg/(ms)}$. The length of the flat plate is $L = 0.2 \, \text{m}$, and the computational domain is extended to $x = -0.02 \, \text{m}$ with the symmetry condition at $y = 0 \, \text{m}$ for numerical robustness. As shown in Fig. 3(a), a slot of periodic suction–blowing perturbation is introduced to the basic flow at the leading edge,

$$q_w(x,t) = \varepsilon \sin \left(2\pi \frac{x - x_1}{x_2 - x_1} \right) \sin (2\pi ft), \quad x_1 \le x \le x_2. \tag{11}$$

Here, q_w is the normal mass flow rate, $x_1 = 0.01 \, \text{m}$, and $x_2 = 0.015 \, \text{m}$. The forcing amplitude $\varepsilon = 0.001$ is adopted to ensure the small disturbance assumption. The forcing frequency f is fixed at 138.74 kHz for all cases, and at this frequency, the Mack second mode is excited at $x > 0.1 \, \text{m}$.[42] In our previous research,[40] we applied Doak's MPT method to analyze the contributions of the source terms to the growth of the second mode in Mach 6.0 boundary layer with different wall temperatures, Reynolds numbers, and disturbance frequencies. The results indicate that the observations and conclusions are general and convincing for the different flow conditions.

For the acoustic metasurfaces, a coating corrugated with subwavelength microslits was placed at $x = 0.12$–$0.18 \, \text{m}$. The geometric parameters for the three types of metasurfaces are listed in Table I. The absorptive metasurface[43] [Fig. 3(b)] and the impedance-near-zero one[25] [Fig. 3(c)] were optimized to achieve a minimum reflection coefficient and a minimum acoustic impedance by searching the geometric parameters space at the corresponding frequency, respectively. The reflection-controlled one[26] was designed with subwavelength groove groups to tune reflection wave propagation upstream based on the generalized Snell's law.

The computational grid has 4950×200 nodes clustered at the leading edge and the plate surface after a grid independence study.[17] For absorptive and impedance-near-zero metasurface, cavities are meshed with a grid dimension of 20×80 (width $\times$ depth) and 32×28 for every cavity, respectively. For the reflection-controlled one,
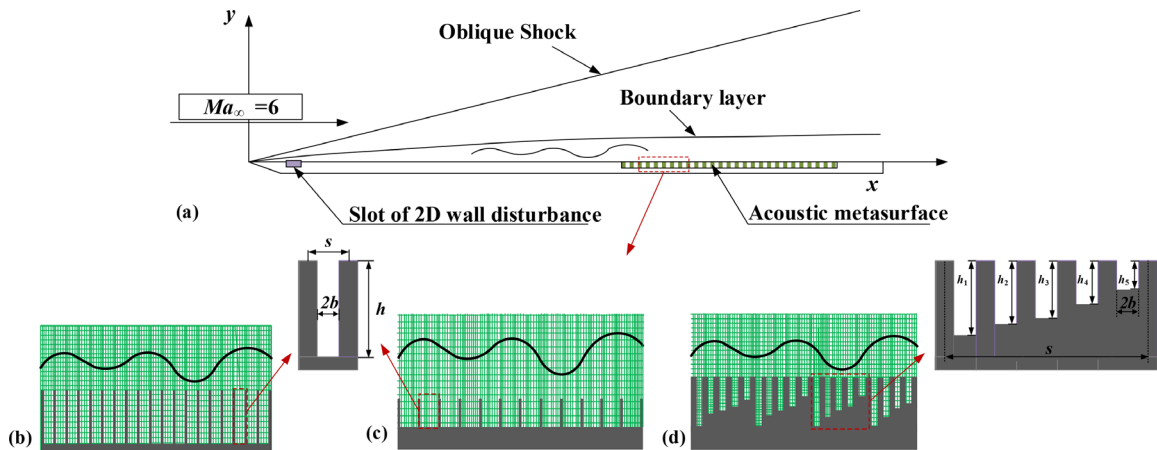

FIG. 3. Schematic drawing of the problem formulation: (a) HBL flow and computational grids among the microslits for (b) an optimized absorptive metasurface,[43] (c) an impedance-near-zero metasurface,[25] and (d) a reflection-controlled metasurface.[26]

TABLE I. Geometric parameters for the three types of metasurfaces.

Cases	Width ($2b \times 10^{-3}$ m)	Depth ($h \times 10^{-3}$ m)	Porosity (n)
Absorptive[43]	3.92	1.63	0.76
Impedance-near-zero[25]	8.32	0.56	0.80
Reflection-controlled[26]	3.92	1.06, 0.79, 0.63, 0.47, and 0.26	0.79

the shallowest slit has a grid dimension of 15×13 (width $\times$ depth), while the deepest slit has a grid dimension of 15×52. A high-order-accurate shock-fitting finite difference method was used to numerically solve the governing equations. The inviscid flux derivatives were discretized using a fifth-order upwind compact scheme, while the viscous terms were discretized using a sixth-order central difference scheme. A third-order Runge–Kutta method was applied for temporal integration, and this code was parallelized using the MPI library.

## III. ACOUSTIC CHARACTERISTICS AND STABILIZATION EFFECTS

A. Comparisons of acoustic characteristics

Before considering the hypersonic flow field, we perform full-wave finite element simulations to compare the acoustic characteristics of the different metasurfaces in quiescent air. For completeness, the contours of all kinds of surfaces are presented below, although Figs. 4(a) and 4(d) have been reported in the previous literature.[26] The operating frequency is $f = 138.74$ kHz, and the angle of the incident

wave is assumed to be $\theta_i = 0°$, i.e., normal to the surface. The incident acoustic waves have the same amplitude in all cases, and by which the scattered acoustic pressure is normalized. The acoustic pressure on the optimized absorptive metasurface [Fig. 4(b)] is minimal, two orders of magnitude smaller than that on the other metasurfaces. The acoustic pressure amplitudes on the other two metasurfaces are similar and slightly lower than that on the rigid surface because of insufficient viscous dissipation. For the impedance-near-zero metasurface, a minimum pressure amplitude can be observed at the surface due to the out-of-phase behavior between the incident and reflected waves. The pressure field pattern of the reflection-controlled metasurface [Fig. 4(d)] is quite different from that of the other metasurfaces, and the reflected waves propagate upstream parallel to the surface because of the linearly changed acoustic phase of the microslits. These wave-front manipulation characteristics were all verified to successfully restrain the Mack second mode.[25,26,43]

B. Comparisons of DNS results

The DNS simulations of the HBL flows on various acoustic metasurfaces had been performed in our previous studies.[25,26,43] The instantaneous fluctuating pressure contours for all cases are compared in Fig. 5. The typical "two-cell" structure is observed on the rigid surface in Fig. 5(a). The fluctuations are considerably amplified downstream ($x > 0.1$ m), indicating the dominance of the Mack second mode. However, on the acoustic metasurfaces, the typical "two-cell" patterns are changed in different ways. For the absorptive metasurface [Fig. 5(b)], the upper mode cells tend to fuze with the lower mode cells and the trailing legs sink into the microslits. For the impedance-near-zero metasurface [Fig. 5(c)], a minimum value appears at the surface
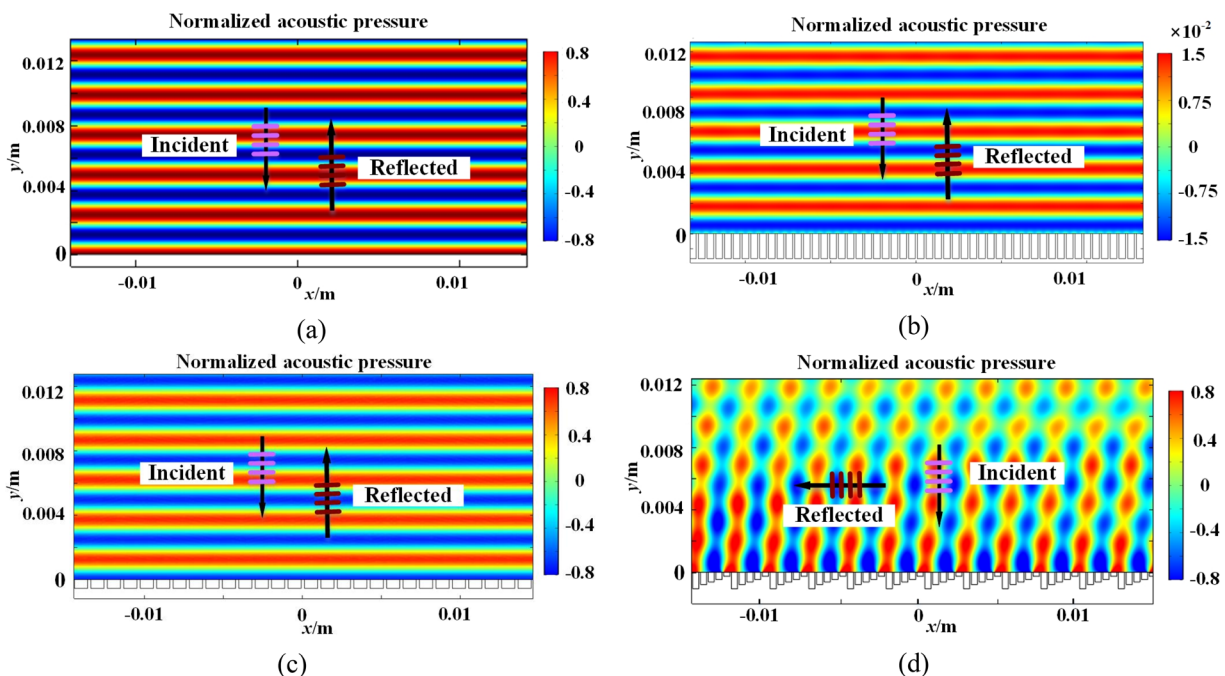
FIG. 4. Normalized scattered pressure fields for various acoustic metasurfaces in the absence of hypersonic fluid flow: (a) rigid surface, (b) absorptive metasurface, (c) impedance-near-zero metasurface, and (d) reflection-controlled metasurface.
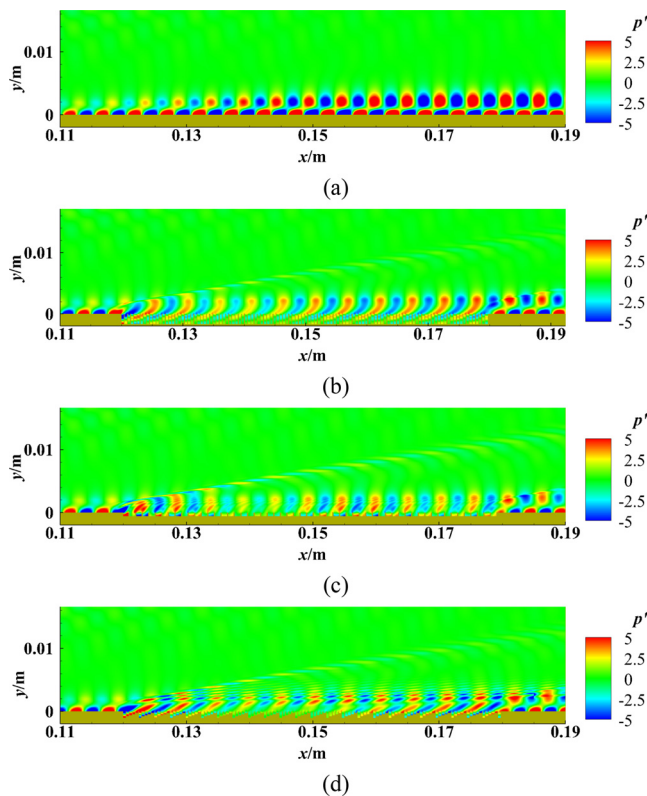
FIG. 5. Fluctuating pressure contours for (a) rigid surface, (b) absorptive metasurface, (c) impedance-near-zero metasurface, and (d) reflection-controlled metasurface (unit: Pa).

as a result of the phase opposition of the instability waves, and the mode structure is divided in the slit and above the surface. For the reflection-controlled metasurface, the mode structures are divided into several segments in the normal direction as shown in Fig. 5(d). The amplitudes of the fluctuating pressure at the wall are shown in Fig. 6. Although the mode structures differ in various ways, for all three metasurfaces, the intensities of the Mack second mode are obviously
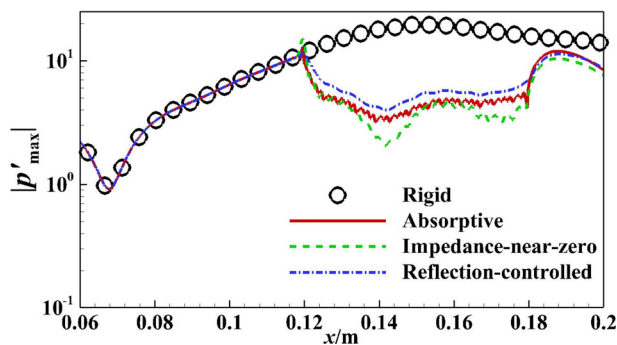

FIG. 6. Comparisons of the maximum fluctuating pressure amplitude along the wall for various surfaces (unit: Pa).

weakened, and the maximum amplitudes of the fluctuating pressures at the wall are significantly reduced.

## IV. INTERPRETATION OF STABILIZATION MECHANISMS

A. MPT decomposition

The different components are extracted by applying Doak's MPT approach to the instantaneous fluctuation fields. Snapshots of the magnitudes of the acoustic component ($\|\boldsymbol{m}'_A\|$), vortical component ($\|\boldsymbol{m}'_B\|$), and thermal component ($\|\boldsymbol{m}'_T\|$) of the rigid surface and absorptive metasurface are depicted in the left column and the right column of Fig. 7, respectively. For 2D vector $\boldsymbol{q} = (q_1, q_2)$, $\|\boldsymbol{q}\| = \sqrt{q_1^2 + q_2^2}$ represents the Euclidean norm of the $\boldsymbol{q}$ vector. In the MPT framework, the Mack second mode has the largest magnitudes of vortical perturbation and the smallest magnitudes of acoustic perturbation. Its thermal perturbation is confined within the BL. The decomposition result agrees well with the result of Ref. 37. Above the absorptive metasurface, all components are suppressed to varying degrees. The expansion wave associated with the juncture between the rigid surfaces and the metasurfaces ($x = 0.12$ m) induces radiations of the vortical and acoustic components. The component contours of the impedance-near-zero and reflection-controlled metasurfaces are nearly identical to those of the absorptive metasurface, and will not be repeated here. To clarify the differences of stabilization mechanism of various metasurfaces, the source contributions to growth rate of disturbances and the corresponding source terms are calculated and analyzed in Secs. IV B and IV C.

B. Source contributions to the growth rate of the Mack second mode

Figure 8 presents the streamwise distributions of growth rate σ and its components contributed by each source term based on the DNS results. Similar to the LST results in Ref. 40, σ_{rta} and σ_{rB} are positive, while σ_{rA} and σ_{rT} are negative. σ_{rta} is the largest component in the region of Mack second mode amplification. σ_{rta} and σ_{rA} are negatively correlated, following a discernible trend of alteration in opposite directions, while σ_{rB} and σ_{rT} are negatively correlated. The sum of the growth rates contributed by all the source terms, σ_r, remains positive in the region of the Mack second mode amplification, indicating that the Mack second mode is unstable on the rigid surface [Fig. 8(a)]. Figure 9 shows the comparison of growth rate for all the cases. In the region of acoustic metasurfaces ($x = 0.12$–0.18), it is observed that the second mode is unstable and three types of metasurfaces suppress the amplification of the second mode effectively. Figures 8(b)–8(d) show the growth rate distributions on the three different acoustic metasurfaces. σ_{mta} and σ_{mA} are negatively correlated, while σ_{mB} and σ_{mT} are negatively correlated, which are consistent with the relationship for the rigid case. σ_{mta} is still the dominant component of the disturbance growth rates contributed by the source terms.

C. Source mechanisms

In this section, the distributions of the source terms are discussed to further explore the stabilization mechanism of different acoustic metasurfaces. Figure 10 shows the contours of the acoustic source terms P_A on various surfaces. Figure 11 shows the normalized distribution of acoustic source for all the cases at $x = 0.135$ m. It is worth
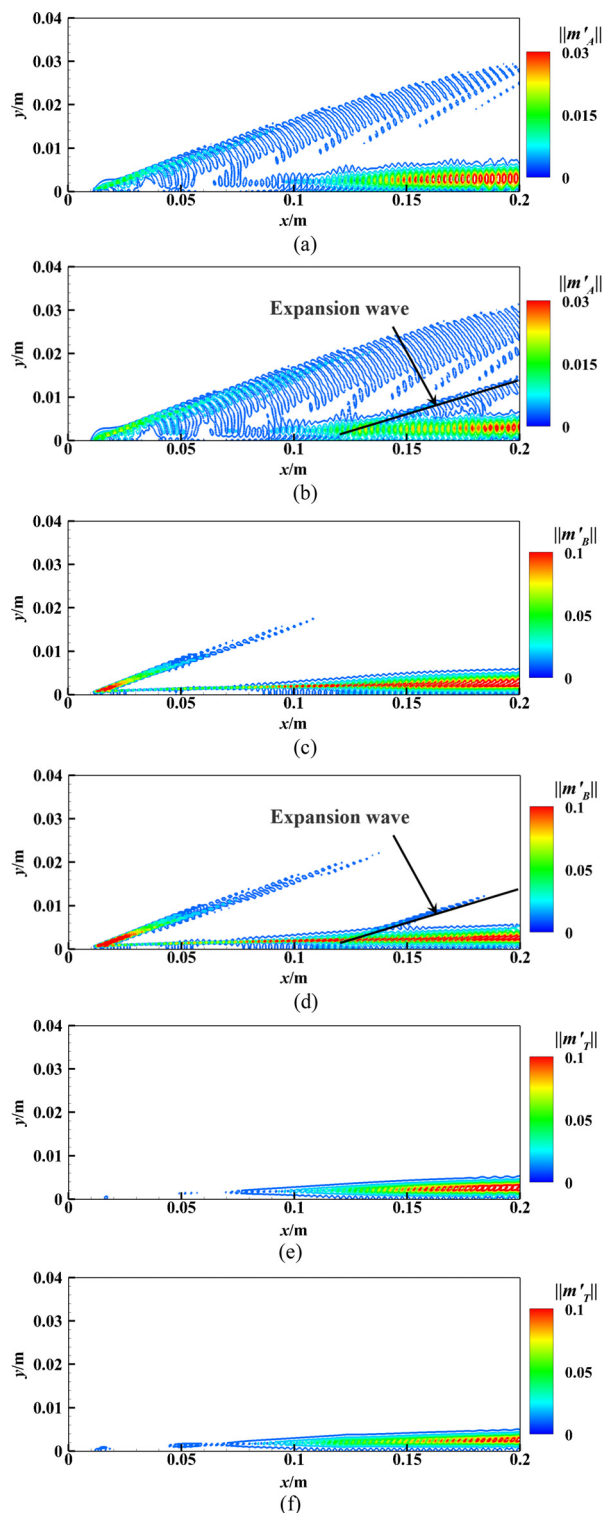
FIG. 7. Magnitudes of (a) and (b) $\boldsymbol{m}'_A$, (c) and (d) $\boldsymbol{m}'_B$, and (e) and (f) $\boldsymbol{m}'_T$ for the rigid surface [(a), (c), and (e)] and the absorptive metasurface [(b), (d), and (f)] [unit: kg/(m^2s)].

noting that a negative source term leads to a positive growth rate and causes instability in the HBL. In most regions, the acoustic source terms are close to zero except near the surface and the critical layer. Above the rigid surface, the acoustic source is negative near the surface, thus destabilizing the Mack second mode. On the other hand, for most of the region near the critical layer, the acoustic source is positive, indicating that it stabilizes the Mack second mode in the HBL. According to Fig. 8(a), σ_{rA} is negative in the entire flow area, implying that the positive acoustic source near the critical layer is dominant. For the three types of acoustic metasurfaces [Figs. 10(b)–10(d)], the negative source near the surface is attenuated by the microslits, whereas the acoustic sources near the critical layer remain positive. It can also be observed that the negative source near the critical layer is enhanced, indicating that the acoustic metasurfaces introduce instability near the critical layer. Since σ_{mA} is generally larger than σ_{rA} in Fig. 8, it can be concluded that acoustic metasurfaces contribute to the instability by enhancing the negative acoustic source near the critical layer.

Figure 12 shows the distributions of the vortical and thermal source terms (P_B and P_T) in the left column and right column, respectively. The wall-normal distributions of the thermal source terms are nearly negatively correlated with the corresponding vortical source terms on both rigid surface and acoustic metasurfaces. The reason for this may be the occurrence of the vortical–entropy coupling effect between $\boldsymbol{m}'_B$ and $\boldsymbol{m}'_T$, as suggested by Crocco's theorem.[37] Similarly, in most regions, the vortical and thermal source terms are nearly zero, except near the surface and the critical layer. For the rigid surface [Fig. 12(a)], the vortical source term P_B is positive near the critical layer and the wall, which stabilizes the Mack second mode. Between the critical layer and the wall, the vortical source term P_B is negative and, therefore, destabilizes the Mack second mode. Since σ_{rB} is positive in Fig. 8(a), the negative vortical source is most significant. For all the acoustic metasurfaces, the positive region of P_B at the near wall is considerably reduced due to the microslits on the wall, and the negative zone between the wall and the critical layer is weakened. As shown in Fig. 8, σ_{mB} is larger than σ_{rB}, indicating that the acoustic metasurfaces mainly contribute to instability by attenuating the positive source at the near wall. The distributions of the thermal source terms are opposite to each other.

Through the quantitative analyses of the source contributions to the growth rate of the Mack second mode (Fig. 8), it has been demonstrated that the thermal-acoustic source term P_{ta} is critical in the amplification of the Mack second mode. Thus, the effect of microslits on the thermal-acoustic source term is the key to explain the stabilization mechanism of different acoustic metasurfaces. As shown in Fig. 13(a), the dominant negative contours cause growth rate σ_{rta} to be the largest component, and thus, σ_{rta} plays a leading role in the amplification of the Mack second mode. The changes in the source term distribution caused by the various acoustic metasurfaces are quite different. In Fig. 13(b), the absorptive metasurface completely dissipates the negative source near the wall, and the negative source term near the critical layer is also attenuated slightly. The attenuation of the negative P_{ta} term leads to a reduction in σ_{ta}, thus stabilizing the Mack second mode. Above the impedance-near-zero acoustic metasurface [Fig. 13(c)], the negative source near the wall is also completely dissipated. However, a positive region exists below the critical layer. For the reflection-controlled metasurface [Fig. 13(d)], the positive source intertwines along the critical layer and the period is consistent with the
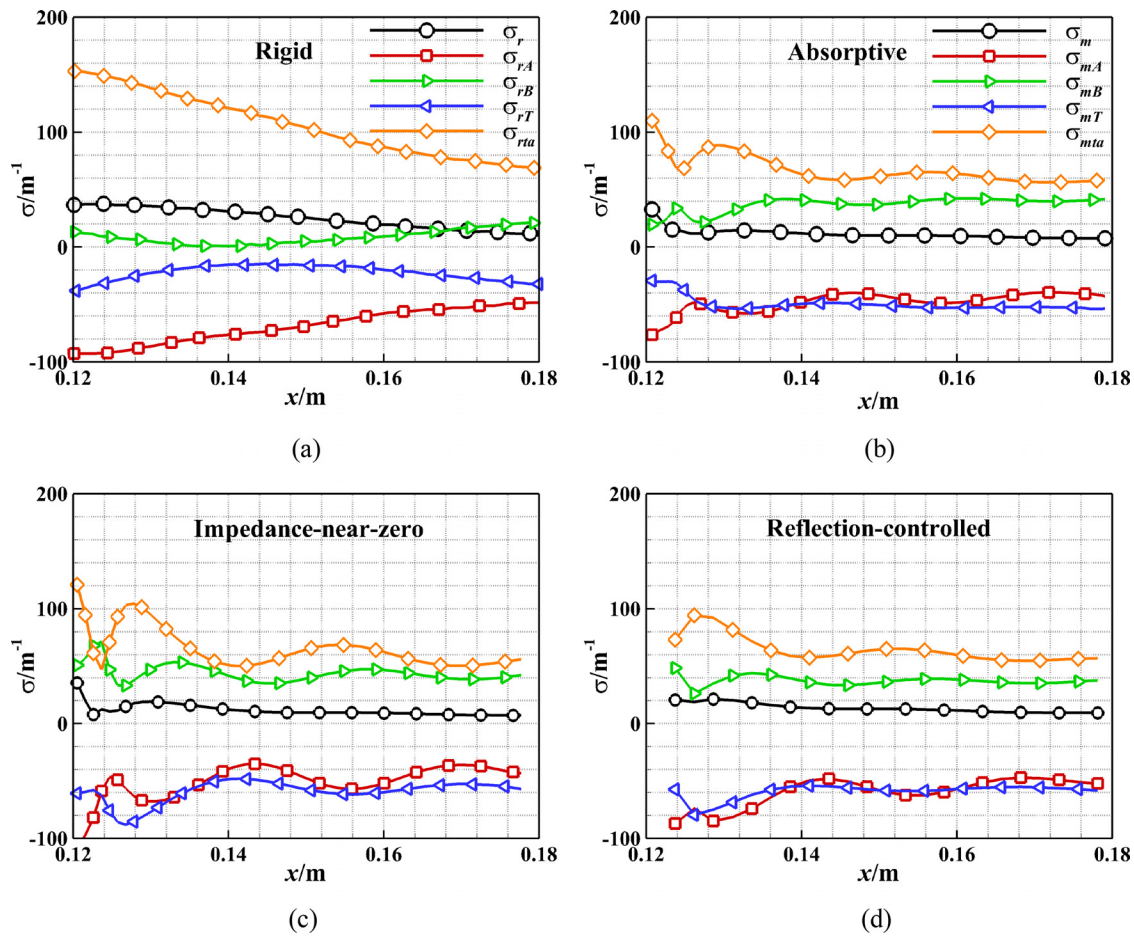
FIG. 8. Streamwise distributions of the growth rate on various surfaces based on the DNS results: (a) rigid surface, (b) absorptive metasurface, (c) impedance-near-zero metasurface, and (d) reflection-controlled metasurface.
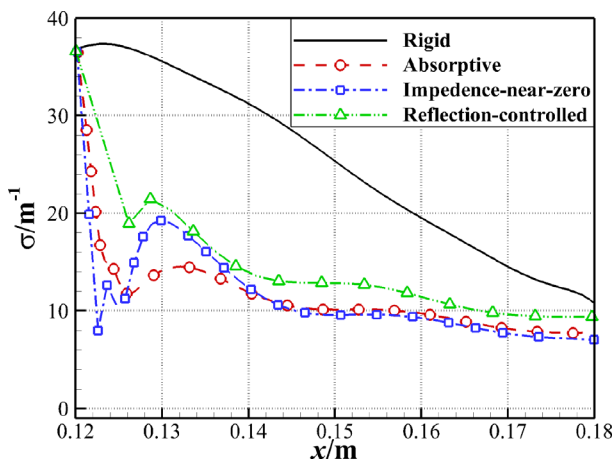

FIG. 9. Comparison of the streamwise distribution of growth rates for all the cases.

distribution period of the slit groups. This indicates that the impedance-near-zero and reflection-controlled metasurfaces affect not only the source terms near the wall but also the source terms near the critical layer.

V. MACROSLITS STABILIZATION MECHANISMS

All of the aforementioned acoustic metasurfaces are corrugated with subwavelength microslits to achieve particular acoustic characteristics. When the slit spacing increases to the same order of magnitude as the disturbance wavelength, the scattered waves at the surface become strong and that will weaken the acoustic ability in the suppression of Mack second mode.[16,42] In this section, the possible stabilization mechanisms of macroslit surfaces will be discussed in the MPT framework. Two kinds of macroslit surfaces are designed: the uniform one and reflection-controlled one with reflection angle of $70°$. Both surfaces have the slits spacing equaling to the wavelength of disturbance of frequency $138.74 \, \text{kHz}$, and the same porosity of $\phi = 0.76$ as the absorptive acoustic metasurface.[43] The uniform one has the depth

13 January 2025 02:57:43
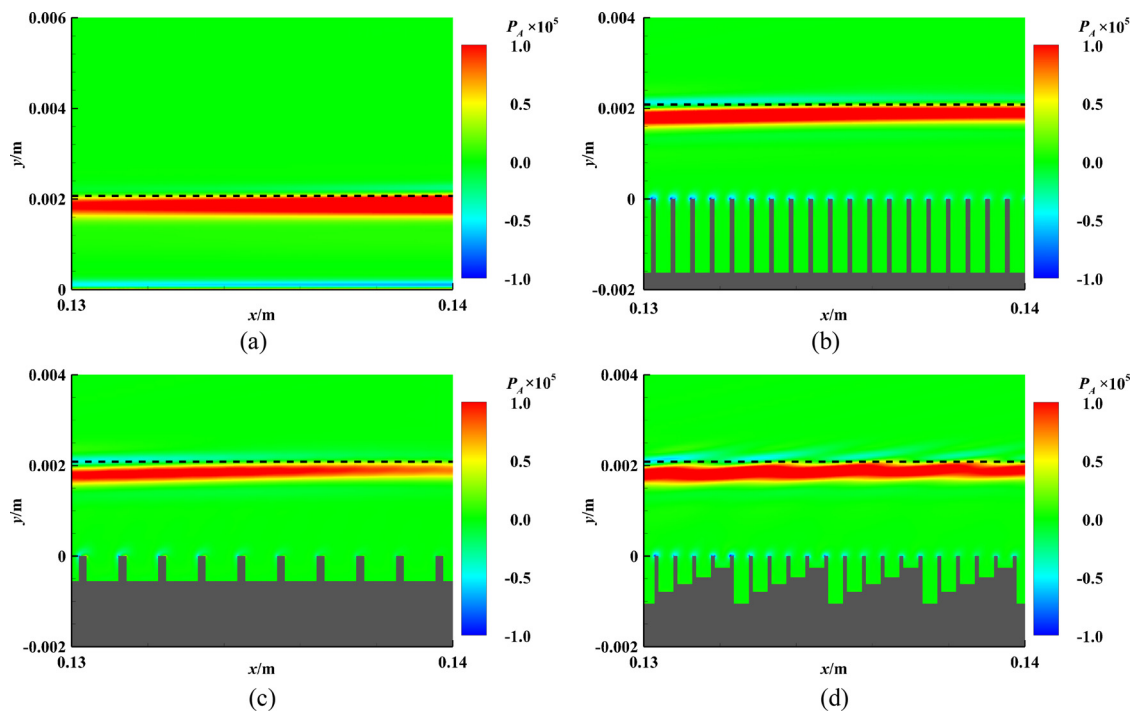
FIG. 10. Acoustic source terms for the: (a) rigid surface, (b) absorptive metasurface, (c) impedance-near-zero metasurface, and (d) reflection-controlled metasurface. The critical layer is indicated by a dashed line [unit: kg/(ms^3)].

$h = 1.34 \times 10^{-3}$ m, while the reflection-controlled one is designed with two slits with different depths in every group ($h_1 = 6.7 \times 10^{-2}$ m and $h_2 = 1.34 \times 10^{-3}$ m). From the steady calculations shown in Fig. 14, compared to that above the metasurfaces,[25,26,43] the macroslit edges induce stronger alternating expansion and compression waves, and the streamlines shows comparatively intensive oscillations near the macroslit surfaces.

Figure 15 shows the instantaneous pressure flowfield from the unsteady calculations. Similar to the contours above the impedance-


FIG. 11. The normalized distribution of acoustic source for all the cases at $x = 0.135$ m [unit: kg/(ms^3)].

near-zero and reflection-controlled metasurfaces depicted in Figs. 5(c) and 5(d), the typical "two-cell" structure of Mack second mode is destroyed on both macroslit surfaces. However, the intensities of fluctuating pressure do not diminish as obviously as those above the metasurfaces. From the comparisons of the maximum fluctuating pressure distributions at the surfaces (Fig. 16), the macroslit surfaces could also suppress the Mack second mode to some extent, and the reflection-controlled surface shows a better stabilization performance than the uniform one.

Figure 17 shows the streamwise distributions of growth rate σ and its components contributed by each source term based on the DNS results. Similar to those of acoustic metasurfaces (Fig. 8), σ_{mta} and σ_{mB} are positive, while σ_{mA} and σ_{mT} are negative. For macroslit cases, σ_{mta} is still the dominant component of the disturbance growth rates contributed by the source terms.

Figure 18 shows the spatial distributions of the thermal-acoustic source term P_{ta} that acts as the dominant factor to excite the unstable Mack second mode. Same as those above the metasurfaces (Fig. 13), the negative P_{ta} near the surfaces is attenuated in the macroslits. The intensive alternating expansion and compression waves induced at the macroslit edges seem affect P_{ta} around the critical layer by producing positive source [Fig. 18(a)]. Compared to the uniform macroslit surface, the reflection-controlled one induces a larger positive P_{ta} that wrapping along the critical layer, which causes a more prominent stabilization performance [Fig. 18(b)]. Including the source mechanisms of acoustic metasurfaces, the recirculation zones inside the slits tend to attenuate the near-surface negative P_{ta} regardless of the slit widths, while the particular acoustic manipulations mainly affect the
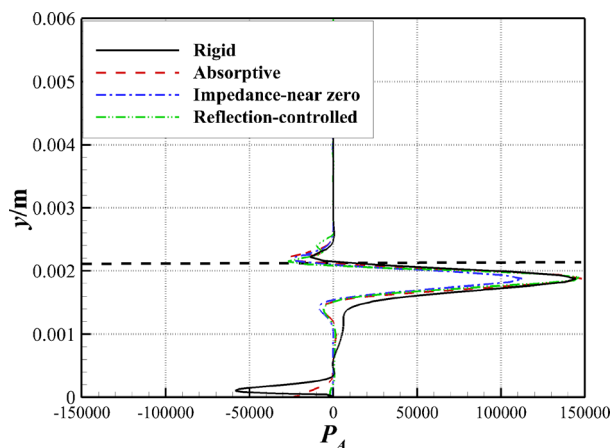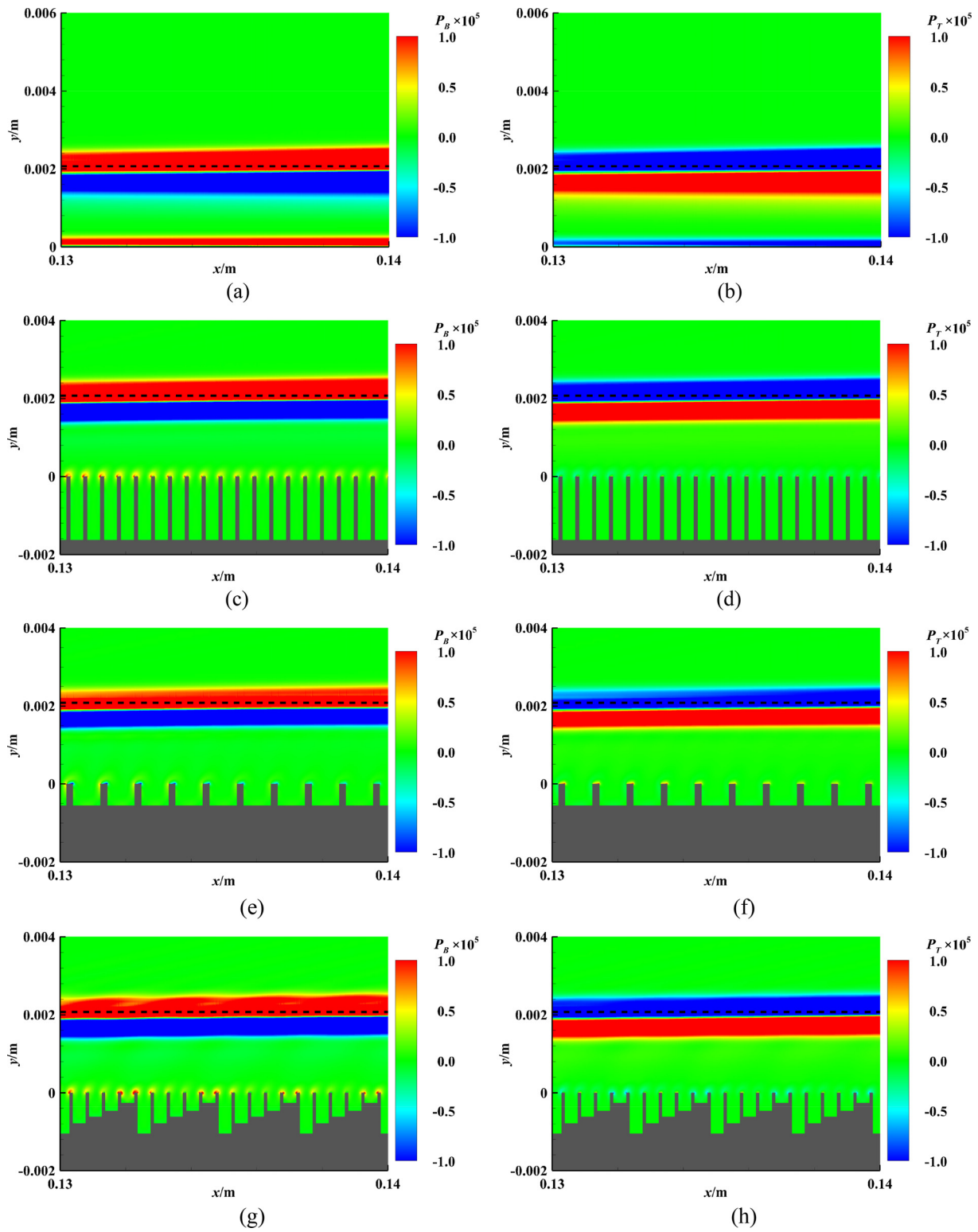
FIG. 12. Vortical source terms (left column) and thermal source terms (right column) for: (a) and (b) rigid surface, (c) and (d) absorptive, (e) and (f) impedance-near-zero, and (g) and (h) reflection-controlled metasurfaces [unit: kg/(ms^3)].
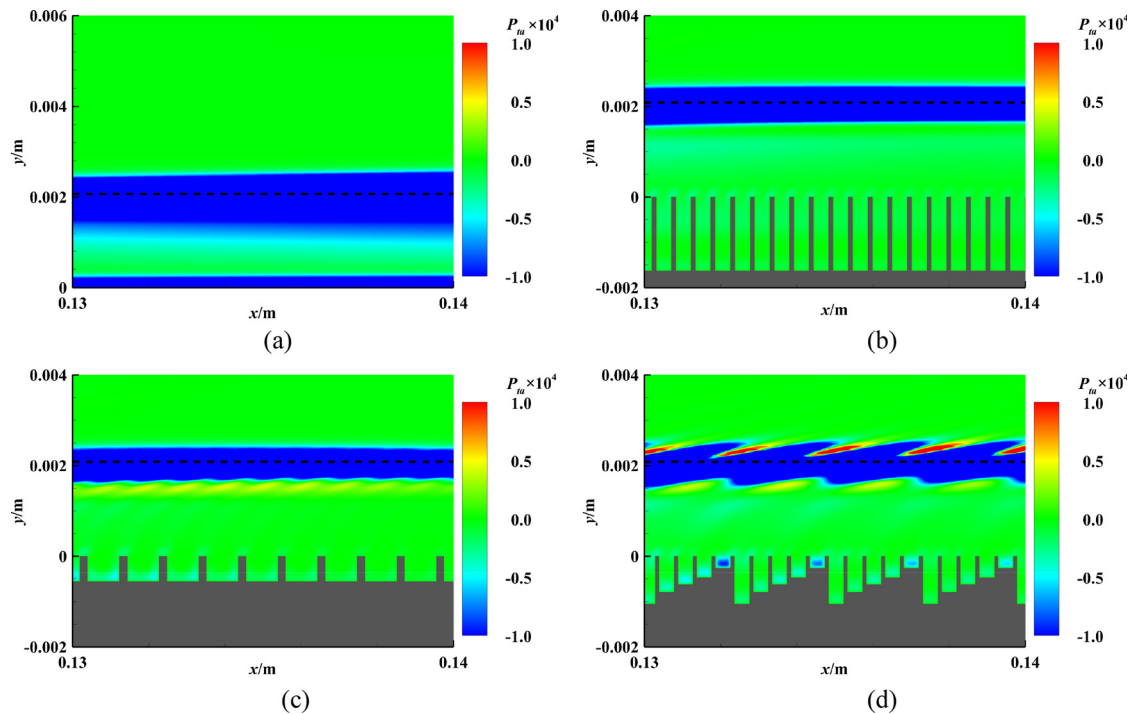
FIG. 13. Thermal-acoustic source terms for: (a) rigid surface, (b) absorptive metasurface, (c) impedance-near-zero metasurface, and (d) reflection-controlled metasurface [unit: $kg/(ms^3)$].

stabilization performance by diminishing negative P_{ta} (the absorptive one) or increasing positive P_{ta} (the impedance-near-zero, reflection-controlled ones, and the reflection-controlled macroslit surface) around the critical layer.

VI. CONCLUSION

The stabilization mechanisms of various acoustic metasurfaces, including the macroslit surfaces, on the Mack second mode in the HBL were clarified within the MPT framework. The relationships

between the commonly defined streamwise growth rates of the unstable modes in the HBL and the source terms in the MPT energy budget equation were established based on the DNS results of acoustic metasurface.

The vortical, acoustic, and thermal components were extracted from the DNS results with MPT decomposition. The vortical component contributes most prominently to the perturbation, while the acoustic component has the smallest contribution. The thermal perturbation is confined in the BL. All the components are suppressed on
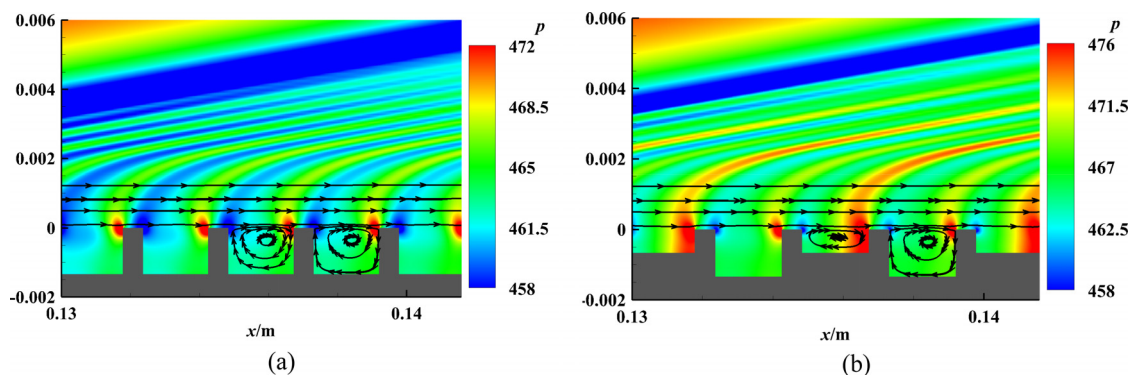
FIG. 14. Local pressure contour around the macroslits for: (a) uniform macroslit surface and (b) reflection-controlled macroslit surface (unit: Pa).
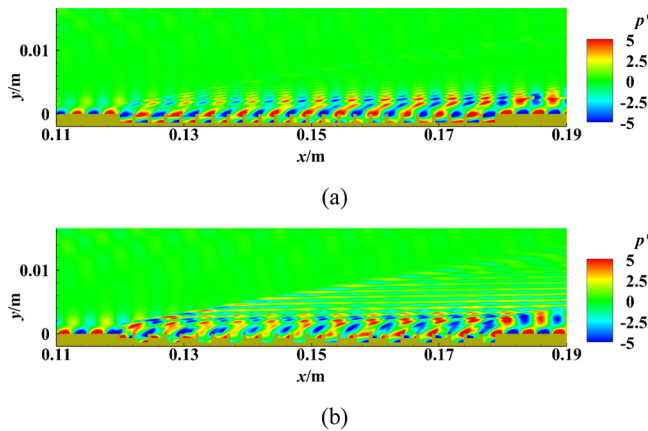
FIG. 15. Fluctuating pressure contours for: (a) uniform macroslit surface and (b) reflection-controlled macroslit surface (unit: Pa).

FIG. 16. Streamwise variation of upper envelope of maximum fluctuating pressure (unit: Pa).

the acoustic metasurfaces. On both rigid surface and acoustic metasurfaces, all the source terms are nearly zero in most flow regions, and the positive/negative source terms that affect the disturbance growth rate are mainly located near the wall and the critical layer. For the various acoustic metasurfaces, the distributions of the vortical, acoustic, and thermal source terms are similar, with the main differences being in the thermal-acoustic source term P_{ta}. The narrow microslits in the absorptive metasurface largely restrain the negative P_{ta} term near the surface and slightly attenuate it near the critical layer. The other two types of metasurfaces mainly strengthen the positive P_{ta} term near the critical layer. The impedance-near-zero metasurface produces a positive contour under the critical layer, while the positive P_{ta} term intertwines along the critical layer above the reflection-controlled metasurface.

Two types of macroslit surfaces with slit spacing equals to disturbance wavelength were introduced to verify the stabilization performances and clarify the inherent mechanisms within the MPT framework. The macroslits induces intensive alternating expansion and compression waves, and slightly caused the BL thinner. The
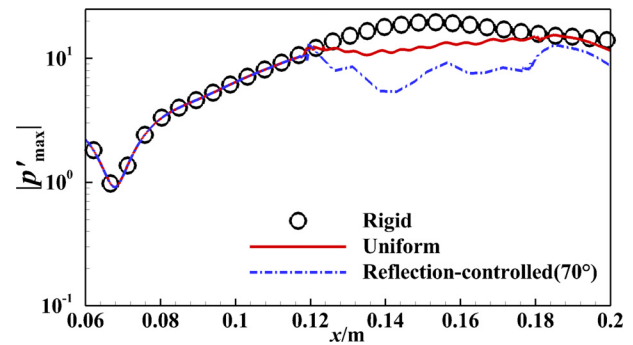
second mode disturbances are suppressed although the scattered waves at the uniform macroslit surface are too strong to represent particular acoustic characteristics. When deflecting the reflection wave to 70°, the stabilization effect become more prominent. By comparing the distributions of P_{ta}, the recirculation zones inside the slits were thought responsible for the attenuation of the near-surface negative P_{ta} regardless of the slit widths, while the acoustic manipulation produces positive source around the critical layer that largely diminishes the growth rate of Mack second model.

The present study not only shows the reduction of the negative thermal-acoustic source term P_{ta} near the surface could affect the amplification of the second mode but also reveals a spatial enhancement of the positive P_{ta} near the critical layer has a similar influence. This spatial wavefront modulation mechanism has been applied to design the reflection-controlled coating with macroslits and that exhibits a better suppression effect and is more conducive to machining in engineering applications. In addition, it suggests a further physical interpretation of the thermal-acoustic source term because of its importance in the amplification of the Mack second mode and also its different behaviors in the metasurface stabilizations. Also, the reasons why there exist negative correlations between different source terms should be clarified in a future study.
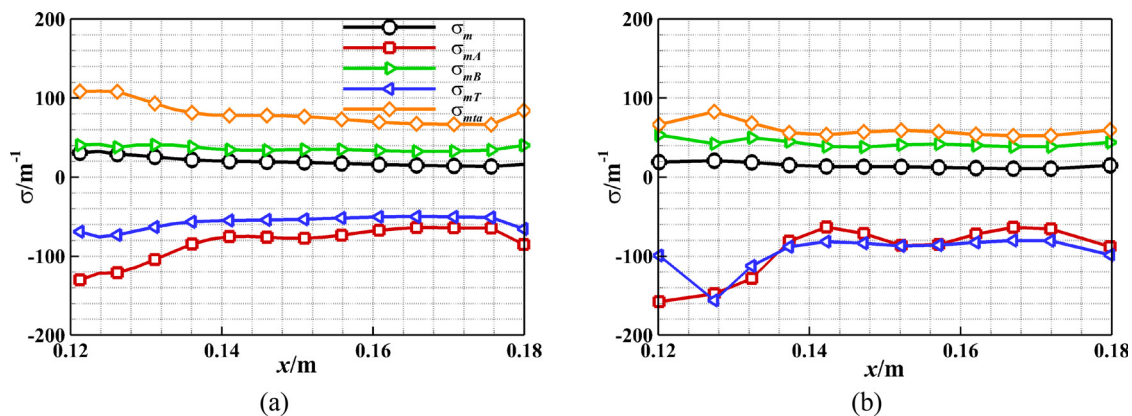
FIG. 17. Streamwise distributions of the growth rate based on the DNS results: (a) uniform macroslit surface and (b) reflection-controlled macroslit surface.
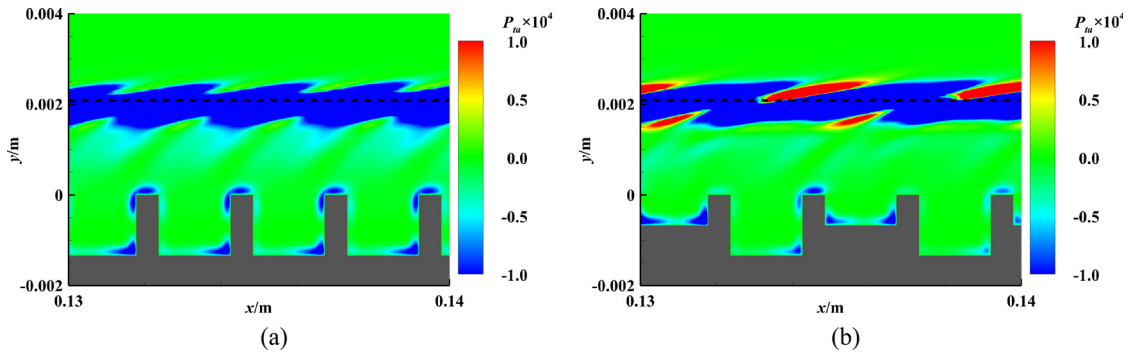
FIG. 18. Thermal-acoustic source term for: (a) uniform macroslit surface and (b) reflection-controlled macroslit surface. The critical layer is marked using a dashed line [unit: $\mathrm{kg}/(\mathrm{ms}^3)$].

AUTHOR DECLARATIONS
Conflict of Interest

The authors have no conflicts to disclose.

Author Contributions

Xiao Liu: Conceptualization (lead); Formal analysis (lead); Writing – original draft (equal). **Ying Dong:** Formal analysis (equal); Software (equal); Writing – original draft (equal). **Tiehan Long:** Formal analysis (equal); Software (equal); Writing – original draft (equal). **Rui Zhao:** Funding acquisition (equal); Supervision (lead); Writing – review & editing (equal). **Chih-Yung Wen:** Funding acquisition (equal); Supervision (equal); Writing – review & editing (equal).

DATA AVAILABILITY

The data that support the findings of this study are available from the corresponding author upon reasonable request.

APPENDIX: MOMENTUM POTENTIAL THEORY

According to the Helmholtz theorem, the vector field $\boldsymbol{m}$ can be split into its rotational component $\boldsymbol{m}_B$ and an irrotational component. The latter can be expressed as a gradient of a scalar potential,

$$\boldsymbol{m} \equiv \rho u = \boldsymbol{m}_B - \nabla \psi, \quad \nabla \cdot \boldsymbol{m}_B = 0. \tag{A1}$$

For a time-stationary flow field, each instantaneous flow quantity consists of a mean part and a fluctuation part,

$$\overline{\boldsymbol{m}} = \overline{\boldsymbol{m}}_B - \nabla \overline{\psi}, \quad \boldsymbol{m}' = \boldsymbol{m}'_B - \nabla \psi'. \tag{A2}$$

The mean continuity equation and the fluctuation continuity equation can be expressed as follows:

$$\nabla \cdot \overline{\boldsymbol{m}} = 0, \quad \frac{\partial \rho'}{\partial t} + \nabla \cdot \boldsymbol{m}' = 0. \tag{A3}$$

The mean momentum density $\overline{\boldsymbol{m}}$ is divergence free. By substituting the corresponding Eq. (A2) into Eq. (A3), the mean scalar potential $\overline{\psi}$ can be assumed to be zero, and a Poisson equation is obtained for the scalar potential of fluctuation,

$$\frac{\partial \rho'}{\partial t} = \nabla^2 \psi'. \tag{A4}$$

For a single-chemical-component continuum in the thermal equilibrium state, the density ρ can be defined as a function of the thermodynamic pressure p and entropy S,

$$\rho = \rho(p, S). \tag{A5}$$

Consequently,

$$\frac{\partial \rho'}{\partial t} = \frac{\partial \rho}{\partial p}\frac{\partial p'}{\partial t} + \frac{\partial \rho}{\partial S}\frac{\partial S'}{\partial t}, \quad \frac{\partial \rho}{\partial p} = \frac{1}{a^2} = \frac{1}{\gamma RT}, \quad \frac{\partial \rho}{\partial S} = -\frac{(\gamma - 1)\rho}{\gamma R}. \tag{A6}$$

Hence, the scalar potential ψ' can be assumed to be a linear superposition of an acoustic potential ψ'_A and a thermal potential ψ'_T,

$$\psi' = \psi'_A + \psi'_T, \quad \frac{1}{\gamma RT}\frac{\partial p'}{\partial t} = \nabla^2 \psi'_A, \quad -\frac{(\gamma - 1)\rho}{\gamma R}\frac{\partial S'}{\partial t} = \nabla^2 \psi'_T. \tag{A7}$$

The fluctuation momentum density $\boldsymbol{m}'$ is, therefore, expressed as a superposition of the vortical component $\boldsymbol{m}'_B$, acoustic component $\boldsymbol{m}'_A$, and thermal component $\boldsymbol{m}'_T$,

$$\boldsymbol{m}' = \boldsymbol{m}'_B + \boldsymbol{m}'_A + \boldsymbol{m}'_T, \quad \boldsymbol{m}_A' = -\nabla \psi'_A, \quad \boldsymbol{m}_T' = -\psi'_T. \tag{A8}$$

In this study, the Poisson equations for ψ' and ψ'_A are solved. Subsequently, ψ'_T and $\boldsymbol{m}'_B$ are obtained using $\psi' - \psi'_A$ and $\boldsymbol{m}' - \boldsymbol{m}'_A - \boldsymbol{m}'_T$, respectively. The Dirichlet boundary conditions for the Poisson equations are formulated by integration along the boundaries, as in Refs. 35 and 40.

13 January 2025 02:57:43

Another critical aspect of Doak's MPT approach is the energy budget for the total fluctuating enthalpy (TFE), $H' = \left(C_p T + \frac{\boldsymbol{u} \cdot \boldsymbol{u}}{2}\right)'$. The mean transport equation of the TFE due to $\boldsymbol{m}'$ can be written as follows:

$$\nabla \cdot \overline{H'\boldsymbol{m}'} = -\overline{\boldsymbol{m}' \cdot \boldsymbol{\alpha}'} + \frac{\overline{p'}}{R}\frac{\partial S'}{\partial t}, \tag{A9}$$

where $\overline{H'\boldsymbol{m}'}$ is the mean TFE flux, representing the TFE transported by $\boldsymbol{m}'$ in a time-stationary process, and the acceleration vector $\boldsymbol{\alpha}'$ is defined as follows:

$$\boldsymbol{\alpha}' = (\boldsymbol{\Omega} \times \boldsymbol{u})' - \left(T\nabla S + \frac{1}{\rho}\nabla \cdot \bar{\bar{\boldsymbol{s}}}\right)', \tag{A10}$$

where $\boldsymbol{\Omega}$ and $\bar{\bar{\boldsymbol{s}}}$ denote the vorticity vector and the viscous stress tensor, respectively. In Eq. (A9), $-\overline{\boldsymbol{m}' \cdot \boldsymbol{\alpha}'}$ is the rate of production or dissipation of the TFE per unit volume due to the interaction between $\boldsymbol{m}'$ and $\boldsymbol{\alpha}'$, and $\frac{\overline{p'}}{R}\frac{\partial S'}{\partial t}$ represents the interaction between fluctuation pressure and fluctuation entropy. The first term in the right-hand side of Eq. (A10) is the fluctuation Lamb vector $(\boldsymbol{\Omega} \times \boldsymbol{u})'$, which represents the effect of vorticity fluctuation. The second and third terms account for the effects of the entropy gradient and viscous stresses, respectively. Because the fluctuation momentum density $\boldsymbol{m}'$ is a superposition of the vortical, acoustic, and thermal components, the terms $H'\boldsymbol{m}'$ and $\boldsymbol{m}' \cdot \boldsymbol{\alpha}'$ can be split into different components of energy flux and the source. Substituting Eq. (A8) into Eq. (A9) yields

$$\frac{\partial \overline{(\rho u)'H'}}{\partial x} + \frac{\partial \overline{(\rho v)'H'}}{\partial y} = -\left[\overline{\boldsymbol{m}'_B \cdot \boldsymbol{\alpha}'} + \overline{\boldsymbol{m}'_A \cdot \boldsymbol{\alpha}'} + \overline{\boldsymbol{m}_{T}' \cdot \boldsymbol{\alpha}'}\right] + \frac{\overline{p'}}{R}\frac{\partial S'}{\partial t}. \tag{A11}$$

The left-hand-side terms in Eq. (A11) are the energy flux terms that represent the fluctuation energy transported along the streamwise and normal directions by flow. The first three terms on the right-hand side indicate the various sources of the interaction of the vector $\boldsymbol{\alpha}'$ with different components. For convenience of discussion, the vortical source $-\overline{\boldsymbol{m}'_B \cdot \boldsymbol{\alpha}'}$, acoustic source $-\overline{\boldsymbol{m}'_A \cdot \boldsymbol{\alpha}'}$, and thermal source $-\overline{\boldsymbol{m}'_T \cdot \boldsymbol{\alpha}'}$ are designated as P_B, P_A, and P_T, respectively. In addition to the source terms due to the MPT components, the source term, $\frac{\overline{p'}}{R}\frac{\partial S'}{\partial t}$, is the interaction between fluctuation pressure and entropy. It is noted that fluctuation pressure and entropy are related to the acoustic and thermal components in Eq. (A7), respectively. Thus, the source, $\frac{\overline{p'}}{R}\frac{\partial S'}{\partial t}$, represents the thermo-acoustic coupling effect in the disturbances flow field and is designated as P_{ta}.

REFERENCES

[1]A. V. Fedorov, "Transition and stability of high-speed boundary layers," Annu. Rev. Fluid Mech. **43**, 79–95 (2011).

[2]Q. Li, W. Yuan, R. Zhao, and H. Wei, "Study on effect of aerodynamic configuration on aerodynamic performance of Mars ascent vehicles," Space **2022**, 9790131.

[3]W. Miao, Q. Li, J. Li, J. Zhou, and X. Cheng, "Thermal environment and aeroheating mechanism of protuberances on Mars entry capsule," Space **2021**, 9754068.

[4]H. L. Reed, W. Saric, and D. Arnal, "Linear stability theory applied to boundary layers," Annu. Rev. Fluid Mech. **28**, 389–482 (1996).

[5]W. Zhu, M. Shi, Y. Zhu, and C. Lee, "Experimental study of hypersonic boundary layer transition on a permeable wall of a flared cone," Phys. Fluids **32**, 011701 (2020).

[6]L. M. Mack, "Boundary-layer linear stability theory," AGARD Report No. 709 (1984).

[7]A. V. Fedorov and N. Malmuth, "Stabilization of hypersonic boundary layers by porous coatings," AIAA J. **39**, 605–610 (2001).

[8]N. Malmuth, A. Fedorov, V. Shalaev, J. Cole, A. Khokhlov, "M. Hites, and D. Williams, "Problems in high speed flow prediction relevant to control," AIAA Paper No. 1998–2695, 1998.

[9]A. Rasheed, H. G. Hornung, A. V. Fedorov, and N. D. Malmuth, "Experiments on passive hypervelocity boundary-layer control using an ultrasonically absorptive surface," AIAA J. **40**, 481–489 (2002).

[10]R. C. Triterelli, S. K. Lele, and A. Fedorov, "Stabilization of a hypersonic boundary layer using a felt-metal porous coating," J. Fluid Mech. **769**, 729–739 (2015).

[11]X. Tian, R. Zhao, T. Long, and C. Wen, "Reverse design of ultrasonic absorptive coating for the stabilization of Mack modes," AIAA J. **57**(6), 2264–2269 (2019).

[12]J. K. Xu, J. X. Liu, S. Mughal, P. X. Yu, and J. Q. Bai, "Secondary instability of Mack mode disturbances in hypersonic boundary layers over micro-porous surface," Phys. Fluids **32**, 044105 (2020).

[13]X. Wang and X. Zhong, "Role of the synchronization point on boundary layer stabilization using porous coating," AIAA Paper No. 2008-4382, 2008.

[14]V. Sousa, D. Patel, J. B. Chapelier, V. Wartemann, A. Wagner, and C. Scalo, "Numerical investigation of second-mode attenuation over carbon/carbon porous surfaces," J. Spacecr. Rockets **56**(2), 319–332 (2019).

[15]G. A. Brès, T. Colonius, and A. V. Fedorov, "Stability of temporally evolving supersonic boundary layers over micro-cavities for ultrasonic absorptive coatings," AIAA Paper No. 2008-4337, 2008.

[16]G. A. Brès, M. Inkman, T. Colonius, and A. V. Fedorov, "Second-mode attenuation and cancellation by porous coatings in a high-speed boundary layer," J. Fluid Mech. **726**, 312–337 (2013).

[17]R. Zhao, C. Y. Wen, T. H. Long, X. D. Tian, L. Zhou, and Y. Wu, "Spatial direct numerical simulation of the hypersonic boundary-layer stabilization using porous coatings," AIAA J. **57**, 5061–5065 (2019).

[18]R. Zhao, Y. X. Fan, X. Liu, and C. Y. Wen, "Stabilization effect of acoustic metasurfaces on broadband disturbances in a Mach 6 boundary-layer flow," Phys. Fluids **34**, 121706 (2022).

[19]A. Fedorov, V. F. Kozlov, and A. N. Shiplyuk, "Stability of hypersonic boundary layer on porous wall with regular microstructure," AIAA J. **44**(8), 1866–1871 (2006).

[20]A. Wagner, M. Kuhn, J. M. Schramm, and K. Hannemann, "Experiments on passive hypersonic boundary layer control using ultrasonically absorptive carbon–carbon material with random microstructure," Exp. Fluids **54**, 1606–1616 (2013).

[21]S. V. Lukashevich, S. O. Morozov, and A. N. Shiplyuk, "Experimental study of the effect of a passive porous coating on disturbances in a hypersonic boundary layer 2: Effect of the porous coating location," J. Appl. Mech. Tech. Phys. **57**(5), 873–878 (2016).

[22]W. Zhu, X. Chen, Y. Zhu, and C. Lee, "Nonlinear interactions in the hypersonic boundary layer on the permeable wall," Phys. Fluids **32**, 104110 (2020).

[23]A. V. Fedorov, A. N. Shiplyuk, A. A. Maslov, E. Burov, and N. D. Malmuth, "Stabilization of a hypersonic boundary layer using an ultrasonically absorptive coating," J. Fluid Mech. **479**, 99–124 (2003).

[24]J. Turner, M. Hoerschgen, W. Jung, A. Stamminger, and P. Turner, "Hypersonic re-entry flight experiment vehicle and subsystem design, flight performance and prospects," AIAA Paper No. 2006-8115, 2006.

[25]R. Zhao, T. Liu, C. Y. Wen, J. Zhu, and L. Cheng, "Impedance-near-zero acoustic metasurface for hypersonic boundary-layer flow stabilization," Phys. Rev. Appl. **11**, 044015 (2019).

[26]R. Zhao, Y. Dong, X. Zhang, C. Wen, T. Long, and W. Yuan, "Control of reflected waves with acoustic metasurfaces for hypersonic boundary-layer stabilization," AIAA J. **59**, 1533 (2021).

[27]Y. Li, B. Liang, Z. M. Gu, X. Y. Zou, and J. C. Cheng, "Reflected wavefront manipulation based on ultrathin planar acoustic metasurfaces," Sci. Rep. **3**, 2546 (2013).

[28]Y. Xie, W. Wang, H. Chen, A. Konneker, B. I. Popa, and S. A. Cummer, "Wavefront modulation and subwave-length diffractive acoustics with an acoustic metasurface," Nat. Commun. **5**, 5553 (2014).

[29]G. Ma, M. Yang, S. Xiao, Z. Yang, and P. Sheng, "Acoustic metasurface with hybrid resonances," Nat. Mater. **13**, 873 (2014).

[30]Y. Cheng, C. Zhou, B. G. Yuan, D. J. Wu, Q. Wei, and X. J. Liu, "Ultra-sparse metasurface for high reflection of low-frequency sound based on artificial Mie resonances," Nat. Mater. **14**, 1013 (2015).

[31]Y. Li and B. M. Assouar, "Acoustic metasurface-based perfect absorber with deep subwavelength thickness," Appl. Phys. Lett. **108**, 063502 (2016).

[32]L. Kovásznauy, "Turbulence in supersonic flow," J. Aeronaut. Sci. **20**, 657–682 (1953).

[33]P. E. Doak, "Momentum potential theory of energy flux carried by momentum fluctuations," J. Sound Vib. **131**, 67–90 (1989).

[34]P. E. Doak, "Fluctuating total enthalpy as the basic generalized acoustic field," Theor. Comput. Fluid Dyn. **10**, 115–133 (1998).

[35]S. Unnikrishnan and D. V. Gaitonde, "Interactions between vortical, acoustic and thermal components during hypersonic transition," J. Fluid Mech. **868**, 611–647 (2019).

[36]O. Tumuklu, V. Theofilis, and D. A. Levin, "On the unsteadiness of shock–laminar boundary layer interactions of hypersonic flows over a double cone," Phys. Fluids **30**, 106111 (2018).

[37]S. Unnikrishnan and D. V. Gaitonde, "Instability characteristics of cooled hypersonic boundary layers," AIAA Paper No. 2020-0588, 2020.

[38]M. L. Houston, D. A. Cook, and W. Nichols, "Aero-thermal decomposition of hypersonic boundary layer over blunt cone," AIAA-Paper No. 2020-2997, 2020.

[39]T. H. Long, Y. Dong, R. Zhao, and C. Y. Wen, "Mechanism of stabilization of porous coatings on unstable supersonic mode in hypersonic boundary layers," Phys. Fluids **33**(5), 054105 (2022).

[40]T. H. Long, P. X. Guo, R. Zhao, C. Y. Wen, and F. Ji, "Energy growth of vortical, acoustic, and entropic components of the second-mode instability in the hypersonic boundary layer," Phys. Fluids **35**(5), 054104 (2023).

[41]D. Bountin, T. Cchimitov, and A. Maslov, "Stabilization of a hypersonic boundary layer using a wavy surface," AIAA J. **51**(5), 1203–1210 (2013).

[42]R. Zhao, C. Y. Wen, X. D. Tian, T. H. Long, and W. Yuan, "Numerical simulation of local wall heating and cooling effect on the stability of a hypersonic boundary layer," Int. J. Heat Mass Transfer **121**, 986–998 (2018).

[43]R. Zhao, T. Liu, C. Wen, J. Zhu, and L. Cheng, "Theoretical modeling and optimization of porous coating for hypersonic laminar flow control," AIAA J. **56**, 2942–2946 (2018).